Supporting Information

Sequential self-reconstruction of localized Mo species in hierarchical carbon/Co–Mo oxide heterostructures for boosting alkaline hydrogen evolution kinetics and durability

Quan Quan,[1] Xiuming Bu,[1] Dong Chen,[1] Fei Wang,[1] Xiaolin Kang,[1] Wei Wang,[1] You Meng,[1] SenPo Yip,[2] Chuntai Liu,[3] Johnny C. Ho[,1,2,4]*

[1] *Department of Materials Science and Engineering, City University of Hong Kong, Hong Kong SAR 999077, China*
[2] *Institute for Materials Chemistry and Engineering, Kyushu University Fukuoka 816-8580, Japan*
[3] *Key Laboratory of Advanced Materials Processing & Mold (Zhengzhou University), Ministry of Education, Zhengzhou 450002, China*
[4] *State Key Laboratory of Terahertz and Millimeter Waves City University of Hong Kong, Hong Kong SAR 999077, China*

E-mail: johnnyho@cityu.edu.hk

Experimental details

Chemicals and Materials: Cobalt nitrate hexahydrate ($Co(NO_3)_2·6H_2O$), ammonium molybdate tetrahydrate ($(NH_4)_6Mo_7O_{24}·4H_2O$), urea ($CO(NH_2)_2$), and potassium hydroxide (KOH) were purchased from Meryer Chemical Technology CO., Ltd. Acetonitrile (CH_3CN) was purchased from RCI Labscan Ltd. Carbon fiber paper (CFP) was purchased from Fuel Cell Store Co. All the chemicals used throughout this work were an analytic grade or better and were used as received without any further purification. Deionized water (DI water) used in the experiments was obtained from local sources. The natural seawater was collected from Cheung Chau (Hong Kong) with a pH value of ~8.2, which was filtered to remove visible impurities before use.

Synthesis of $CoMoO_4$: $CoMoO_4$ nanosheet arrays supported on CFP were synthesized by a facile solvothermal method. The commercial CFP was cut into a rectangular shape with the size of 1×3 cm^2. The pieces of CFP were sequentially cleaned in acetone, ethanol, and DI water for 15 min by sonication. 0.75 mmol of $Co(NO_3)_2·6H_2O$, 0.25 mmol of $(NH_4)_6Mo_7O_{24}·4H_2O$, and 5 mmol of $CO(NH_2)_2$ were added into 25 mL of DI water. After being stirred for 1 h, the homogenous solution was transferred into a 50 mL Teflon-lined autoclave. Simultaneously, a piece of CFP was tilted in the autoclave, which was then sealed and heated at 180 °C for 12 h. After cooling to room temperature, the CFP was taken

out by a tweezer, rinsed with water thoroughly, and dried at 60 °C in an oven overnight.

Synthesis of Co@NCNT/CoMoO$_x$: The as-prepared $CoMoO_4$ sample supported on CFP was placed in the center of the quartz tube. The air inlet of the tube furnace is connected with a gas washing bottle containing 100 mL of CH_3CN solution. Argon (Ar) flowing with a rate of 100 sccm was applied to bubble through the CH_3CN to create a CH_3CN/Ar atmosphere. Then, the sample was annealed at 600 °C for 2 h with a ramping rate of 20 °C min^{-1}.

Synthesis of Co@NCNT/CoMo$_y$O$_x$: In a standard three-electrode electrolyzer, an Ag/AgCl electrode and a graphite rod were employed as reference and counter electrodes, respectively. The Co@NCNT/CoMoO$_x$ supported on CFP was directly used as a working electrode. The cyclic voltammetry (CV) was conducted on Co@NCNT/CoMoO$_x$ in the potential range from 0 to 0.8 V *vs*. Ag/AgCl at a scan rate of 0.1 V/s with 40 cycles in 1 M KOH. After the *in-situ* anodic oxidation (AO) reaction, the Co@NCNT/CoMo$_y$O$_x$ sample was obtained.

Synthesis of CoO: The synthesis procedure of CoO supported on CFP was the same as that of $CoMoO_4$ except for no addition of $(NH_4)_6Mo_7O_{24}\cdot 4H_2O$.

Synthesis of Co@NCNT/CoO$_x$: The synthesis procedure of Co@NCNT/CoO$_x$ was the same as that of Co@NCNT/CoMoO$_x$ except for using CoO to replace the $CoMoO_4$ counterpart.

Characterizations: The scanning electron microscopy (SEM) was conducted by the FEI Quanta 450 equipment. The transmission electron microscopy (TEM), high-resolution TEM (HRTEM), high-angle annular dark-field scanning TEM (HAADF-STEM), energy-dispersive X-ray spectroscopy (EDS), and elements mapping analysis were conducted by using a JEM-2100F instrument at an accelerating voltage of 200 kV. X-ray diffraction (XRD) patterns were recorded on a Bruker D8 Advance powder diffractometer. X-ray photoelectron spectroscopy (XPS) was carried out on Thermo Fisher ESCALAB 250Xi equipment and all binding energies were calibrated by the C 1s peak at 284.6 eV. The inductively coupled plasma-mass spectroscopy (ICP-MS) was performed on a PE optima 6000 spectrometer.

***In-situ* Raman spectroelectrochemistry**: *In-situ* Raman spectra were measured on Renishaw inVia Reflex microscope under an excitation of 532 nm laser light. The *in-situ* electrochemical cell was made by Teflon with a quartz window to protect the objective. A platinum wire and Ag/AgCl served as the counter and reference electrodes, respectively. The working electrode (diameter: 6 mm; geometric area: ~0.28 cm^2) was set to keep the plane of the sample perpendicular to the incident laser. The Raman spectra were controllably collected at different potentials or time by an electrochemical workstation, respectively. Specifically, the potential is sequentially decreased from –0.05 V to –0.3 V *vs*. RHE from with an increment of −0.05 V. Each potential applied lasts for 10 min. The potentials were carefully set to a certain negative range as the light path was greatly interfered by the evolved hydrogen gas bubbles. All potentials discussed in the results were given against the reversible hydrogen electrode (RHE).

Electrochemical tests: Electrochemical measurements were conducted on a standard three-electrode

system using an electrochemical workstation (CHI 760E). The electrolyte was 1 M KOH (pH = 13.9). For the electrochemical measurement in alkaline seawater, the electrolyte was 1 M KOH + seawater (pH ≈ 13.8). The concentration of NaCl in the natural seawater is about 0.49 M. The sample supported on CFP (1 cm × 3cm) was directly used as a working electrode. The geometric surface area of 1 cm^2 (*i.e.*, 1 cm × 1cm) was immersed into the electrolyte. An Ag/AgCl electrode and a graphite rod were employed as reference and counter electrodes, respectively. For the Pt/C powder as a benchmark sample, 5 mg Pt/C (commercial 20% Pt/C) was dispersed in a mixture of 50 μL Nafion solution (5 wt%) and 450 μL ethanol under sonication for 2 h to form a homogeneous ink. Subsequently, 100 uL ink was drop-casted onto the surface of the CFP (1 cm × 1cm) with a Pt/C mass loading of 1 mg cm^{-2} (*i.e.*, the Pt mass loading of 0.2 mg cm^{-2}) and dried at ambient temperature. Before the electrochemical measurement, the electrolyte was bubbled with Ar flow for 30 min. The linear sweep voltammetry (LSV) was measured at a scan rate of 5 mV s^{-1}. All polarization curves were exhibited with iR correction unless otherwise mentioned. iR correction was performed by the formula: $E_{iR} = E_0 - i \times R_s$, where the solution resistance (*i.e.*, R_s) was measured through electrochemical impedance spectroscopy (EIS). EIS measurement was conducted from 0.01 to 100000 Hz with an amplitude of 5 mV at a potential of −0.19 V. The double-layer capacitance (C_{dl}) was measured by CV cycling at sweep rates of 5 to 25 mV s^{-1}. The long-term stability of catalysts was evaluated using chronoamperometry (CA) and chronopotentiometry (CP) tests without iR compensation. During the reaction, 1 mL of electrolyte was periodically added into the stability-test system for the compensation of water consumption. All potentials were normalized to the RHE according to the Nernst equation: E (*vs*. RHE) = E (*vs*. Ag/AgCl) + 0.0591 V × pH + 0.197 V.

Theoretical computation details: We employed the Vienna Ab Initio Package (VASP)[1,2] to perform all the density functional theory (DFT) calculations within the generalized gradient approximation (GGA) using the PBE formulation.[3] We chose the projected augmented wave (PAW) potentials[4,5] to describe the ionic cores and take valence electrons into account using a plane wave basis set with a kinetic energy cutoff of 450 eV. Partial occupancies of the Kohn−Sham orbitals were allowed to use the Gaussian smearing method and a width of 0.05 eV. The electronic energy was considered self-consistent when the energy change was smaller than 10^{-4} eV. A geometry optimization was considered convergent when the force change was smaller than 0.05 eV/Å. The Brillouin zone integral used the surfaces structures of 2×2×1 monkhorst pack K point sampling for surface structures.

We have performed the geometry optimization for $CoMoO_4$ unit cell and the lattice parameters were 9.760 Å, 8.986Å and 7.816 Å, which was consistent with materials project Crystal Structure Database. For all surface models, we used the three-layers slab with a supercell of (2×2) for (−222) facet as the active surface. The two bottom layers were fixed and the top two layers were allowed to relax with the adsorbates. Periodic boundary conditions were used in all directions and a vacuum layer of 15 Å was used in the z-direction to separate the slabs.

Finally, the adsorption energies (E_{ads}) were calculated as:

$E_{ads} = E_{ad/sub} - E_{ad} - E_{sub}$

where $E_{ad/sub}$, E_{ad}, and E_{sub} are the total energies of the optimized adsorbate/substrate system, the adsorbate in the gas phase, and the clean substrate, respectively.

The free energy (ΔG) for elemental reaction step were calculated as:

$\Delta G = \Delta E + \Delta EZPE - T\Delta S$

where Δ*E* is the difference between the total energy, ΔEZPE and ΔS are the differences in the zero-

point energy and the change of entropy, T is the temperature (T = 300 K in this work), respectively.

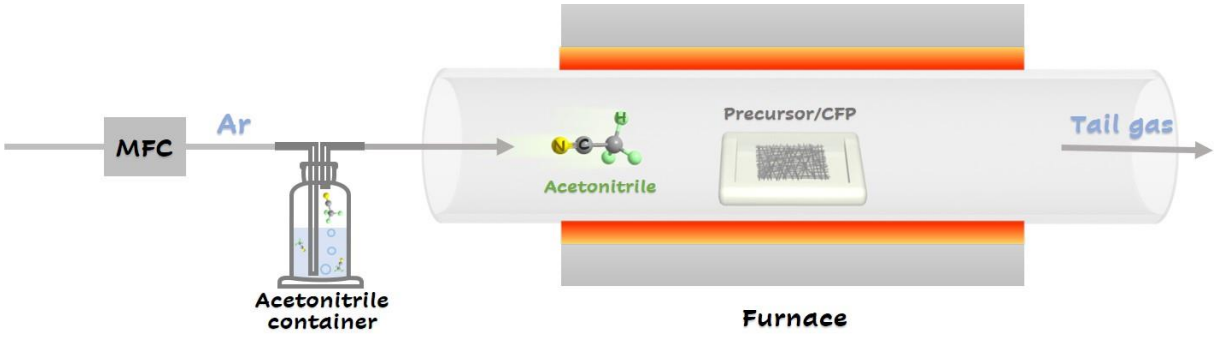

Fig. S1 Schematic illustration of acetonitrile-flow calcination system.

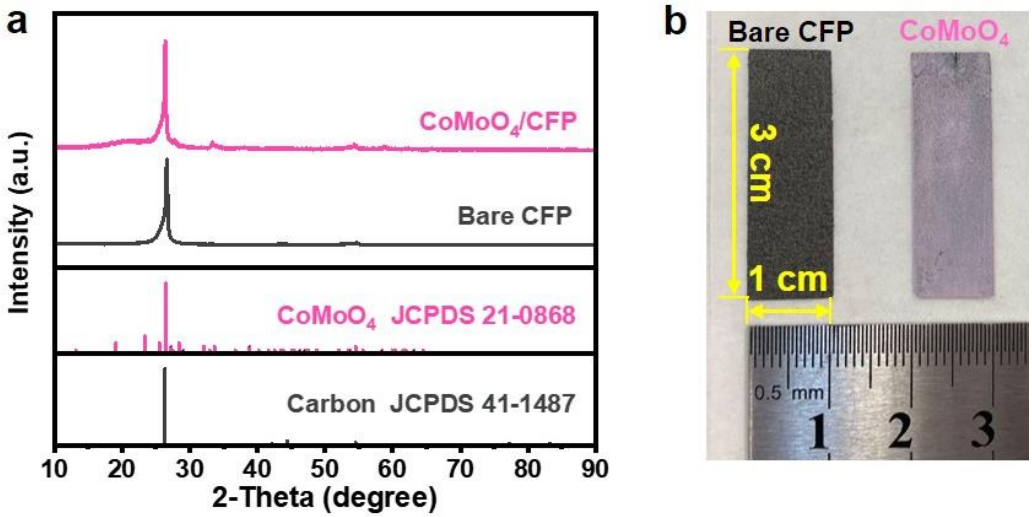

Fig. S2 (a) XRD patterns and (b) digital photographs of bare CFP and $CoMoO_4$/CFP.

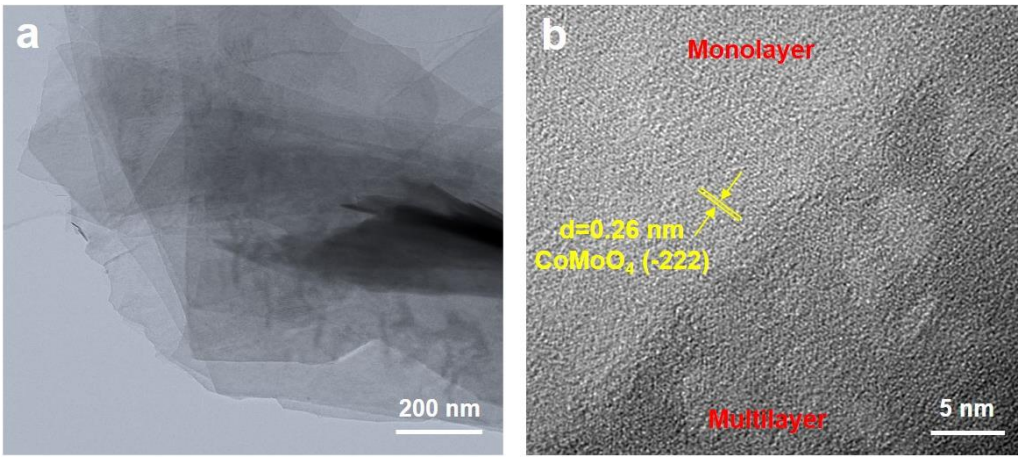

Fig. S3 (a) TEM and (b) HRTEM images of $CoMoO_4$.

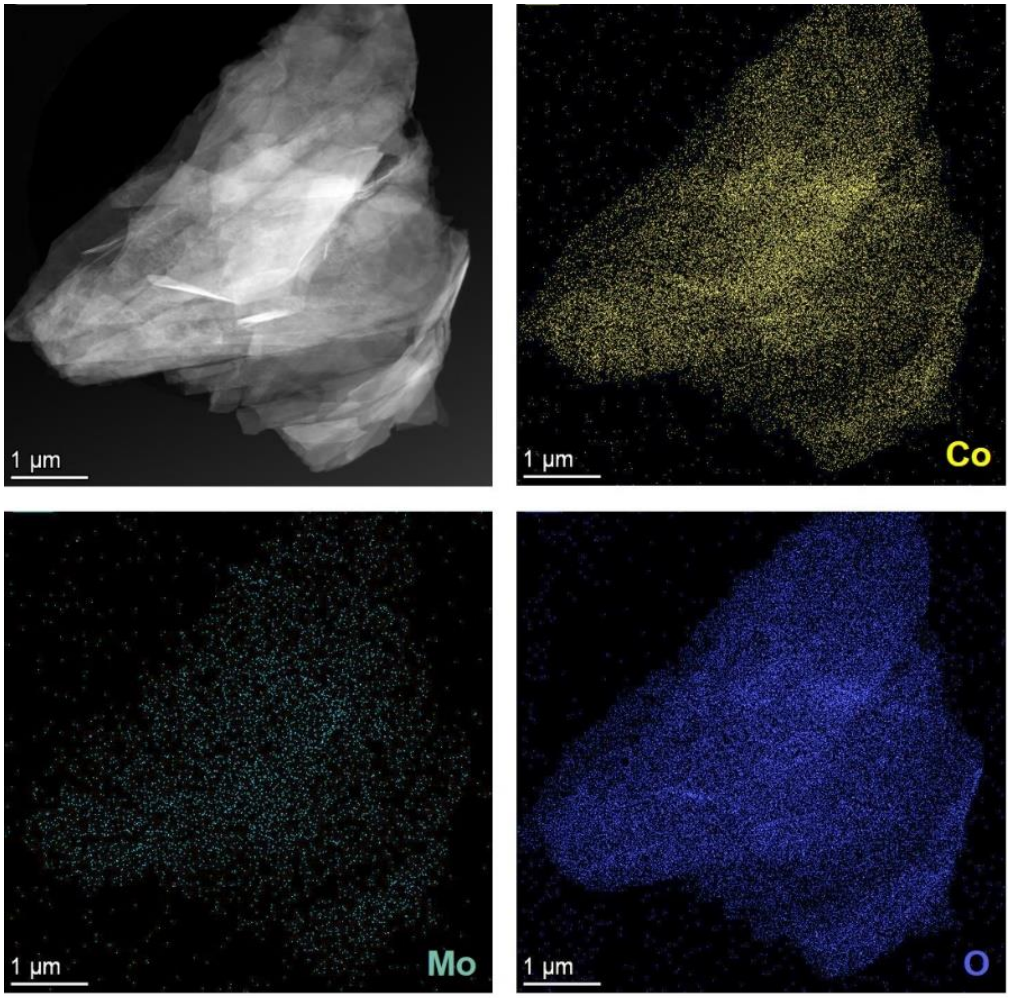

Fig. S4 HAADF-STEM image and elemental mapping of $CoMoO_4$.

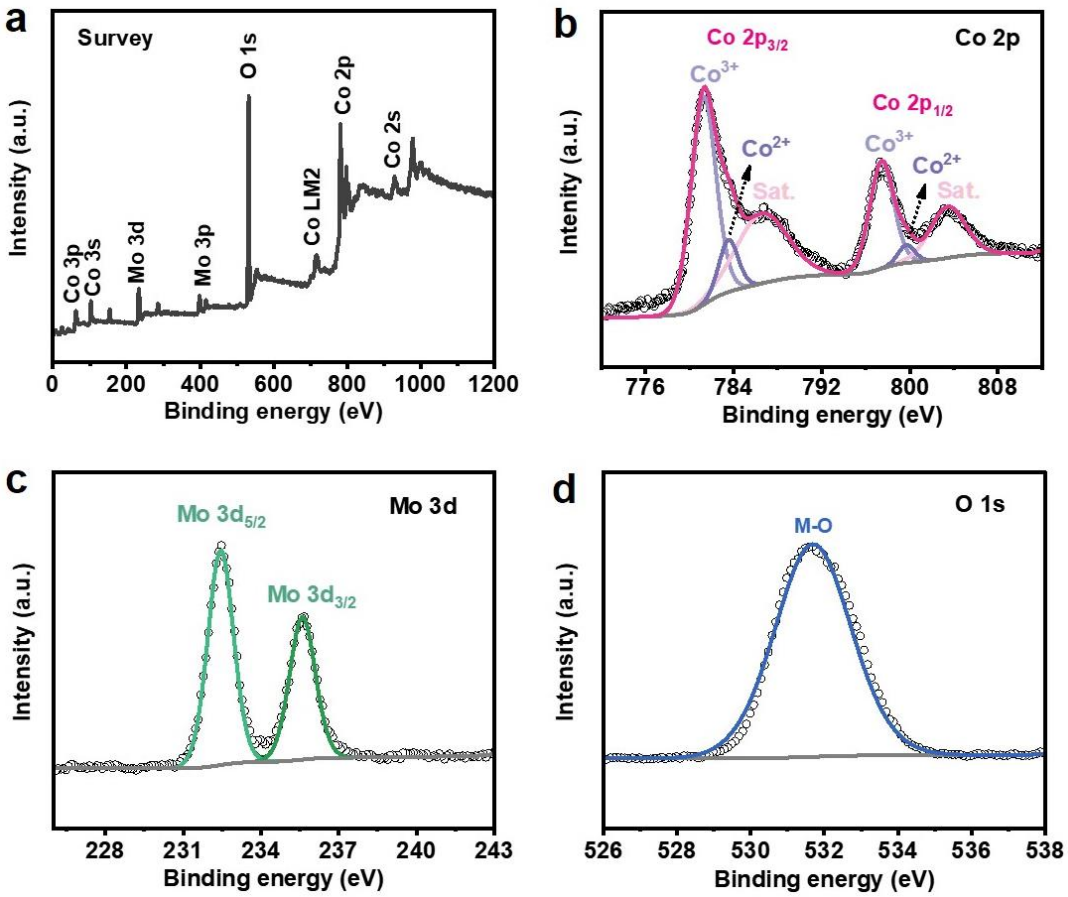

Fig. S5 (a) XPS survey spectrum of $CoMoO_4$ and high-resolution XPS spectra of (b) Co 2p, (c) Mo 3d, and (d) O 1s.

Specifically, the Co^{2+} ($2p_{1/2}/2p_{3/2}$: 799.78 eV/783.58 eV) and Co^{3+} ($2p_{1/2}/2p_{3/2}$: 797.48 eV/781.28 eV) are observed from the Co 2p spectrum while only Mo^{6+} ($2p_{3/2}/2p_{5/2}$: 235.60 eV/232.45 eV) is detected from the Mo 3d spectrum.

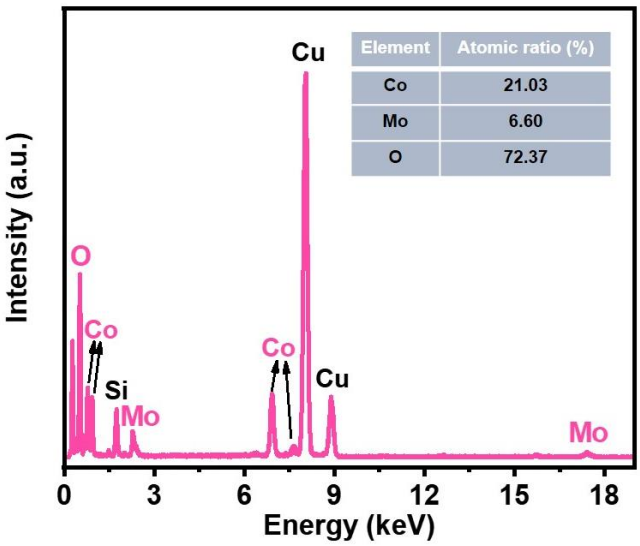

Fig. S6 EDS of $CoMoO_4$ (inset: the atomic ratio of Co, Mo, and O elements).

The results demonstrate the coexistence of Co, Mo, and O elements. It is noted that as the nanosheet structure of the as-prepared $CoMoO_4$ sample is thin, part of the electron beam could directly pass through the sample during a high voltage of TEM-EDS measurement. Although the obtained signal result is limited instead of reflecting the real atomic ratio for quantitative analysis, a large discrepancy between the experimental Co/Mo content ratio and stoichiometry for the $CoMoO_4$ compound (Co/Mo = 1:1) still exists. This result suggests that cobalt in the sample may partly exist in the form of separate amorphous Co oxide, besides its portion in crystalline $CoMoO_4$. In addition, the signals of Si and Cu originate from equipment and copper grid, respectively.

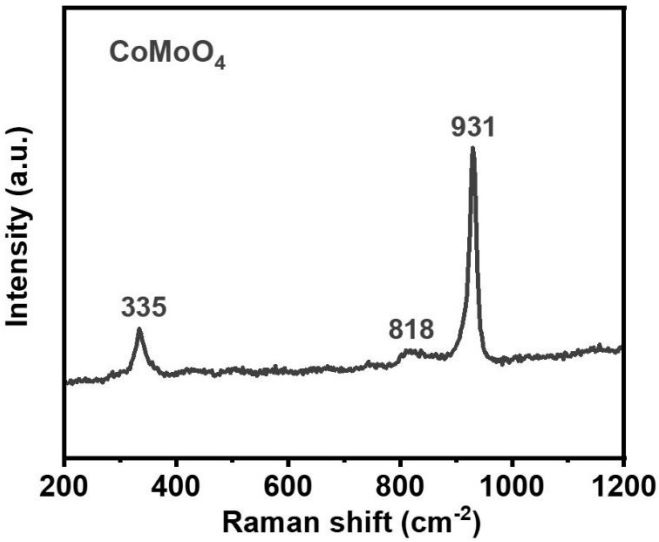

Fig. S7 Raman spectrum of $CoMoO_4$.

For $CoMoO_4$, the peak located at about 335 cm^{-1} corresponds to asymmetric and symmetric bending modes of the O-Mo-O; and the band at around 818 cm^{-1} is related to asymmetric stretching modes of oxygen in binding O-Mo-O. The band located at around 931 cm^{-1} is associated with the symmetric stretching of the Mo=O bonds. Besides, the distinct band belonging to amorphous Co oxide is not detectable, meaning that the separate amorphous Co oxide may exist underneath the surface of $CoMoO_4$ species.

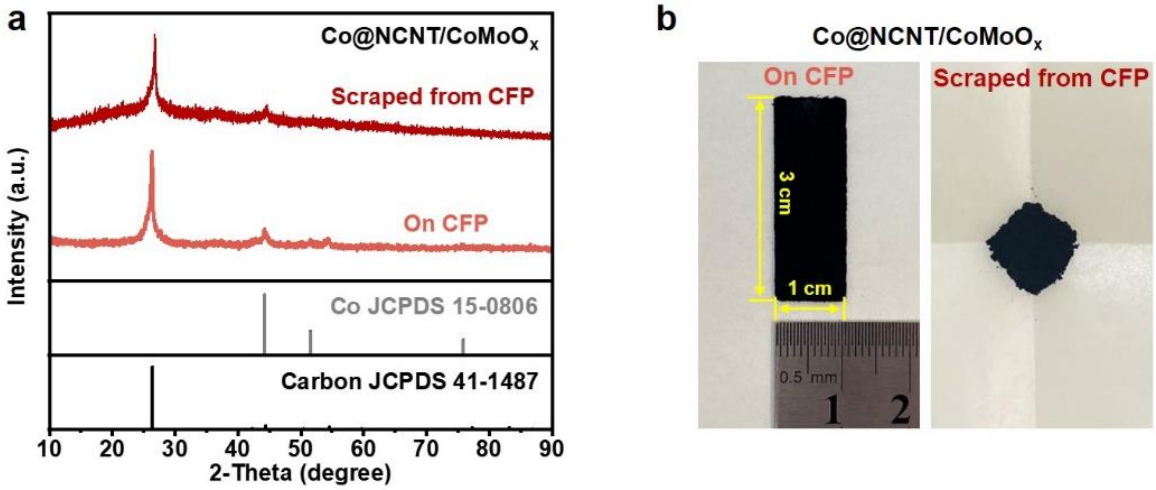

Fig. S8 (a) XRD patterns and (b) digital photographs of Co@NCNT/$CoMoO_x$ grown on CFP and the sample scraped from the CFP substrates.

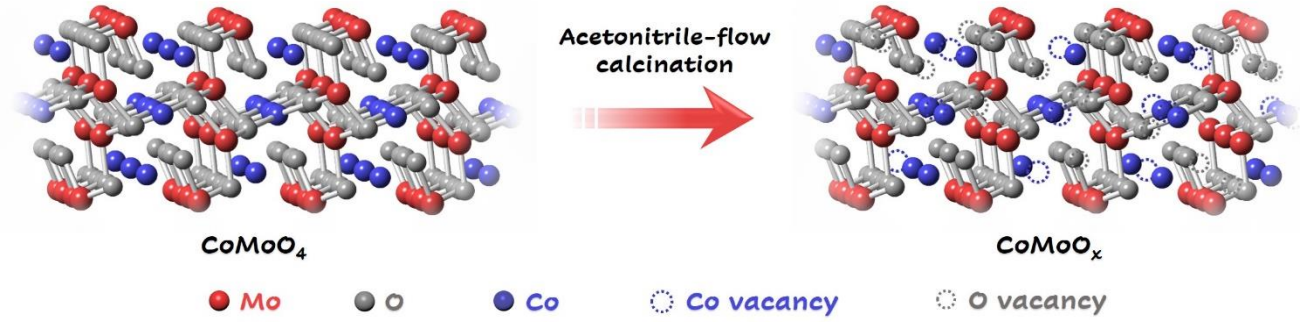

Fig. S9 Schematic diagram of the $CoMoO_4$ crystal structure transformed into $CoMoO_x$.

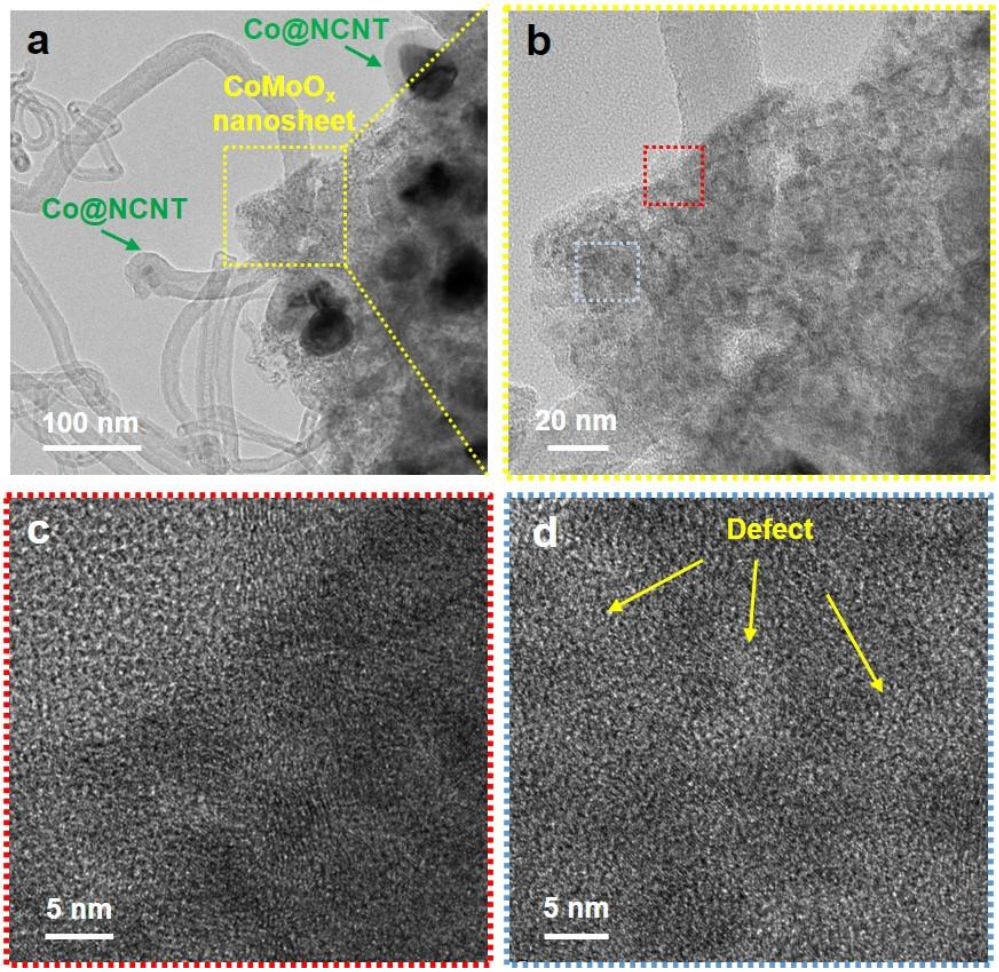

Fig. S10 (a, b) TEM images of Co@NCNT/$CoMoO_x$. (c, d) HRTEM images of the $CoMoO_x$ nanosheets in the selected zones in (b).

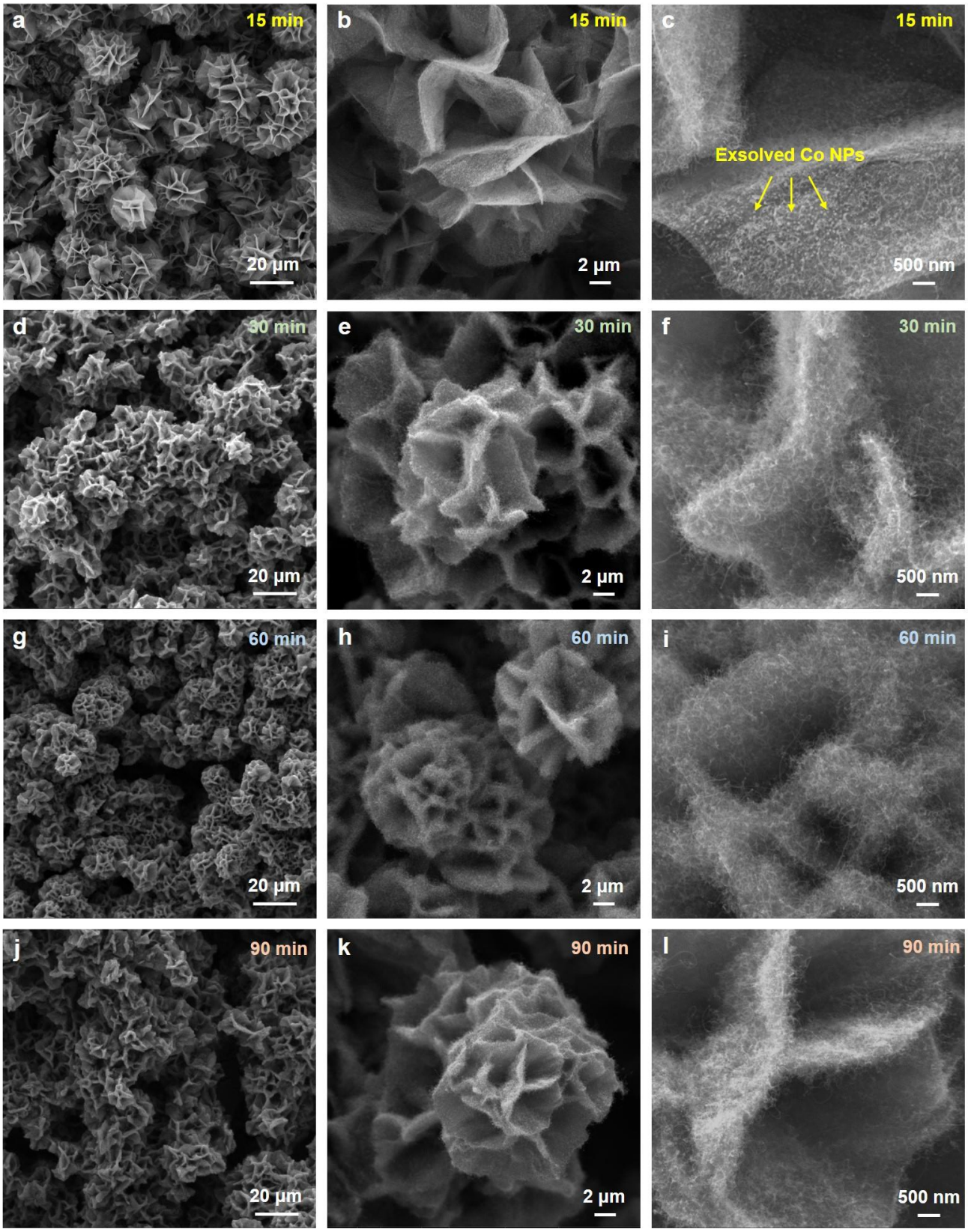

Fig. S11 SEM images of obtained Co@NCNT/$CoMoO_x$ by time-dependent control experiments. (a-c) 15 min, (d-f) 30 min, (g-i) 60 min, and (j-l) 90 min.

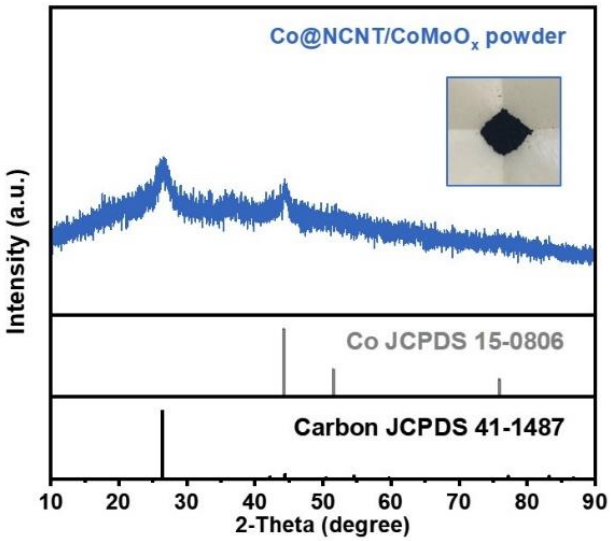

Fig. S12 XRD pattern and a digital photograph of Co@NCNT/CoMoO$_x$ powder.

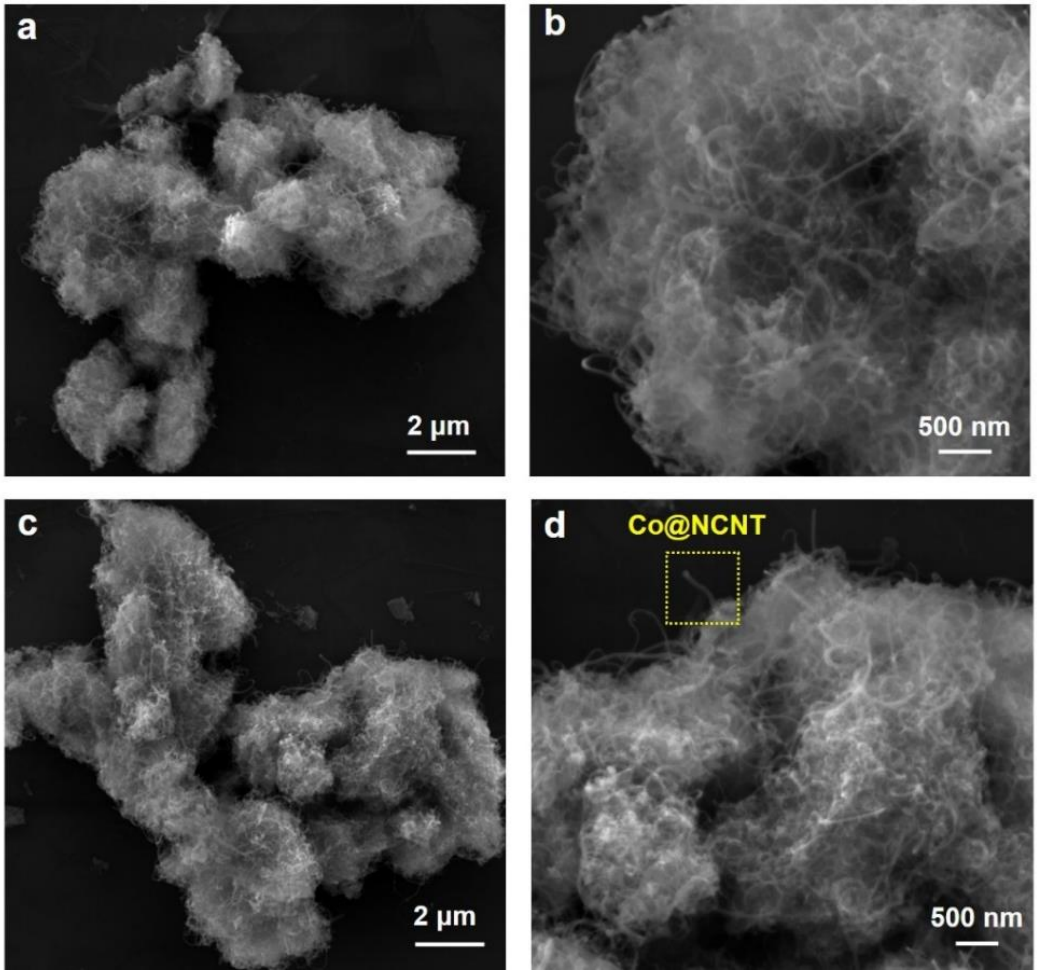

Fig. S13 SEM images of Co@NCNT/CoMoO$_x$ powders at different magnifications.

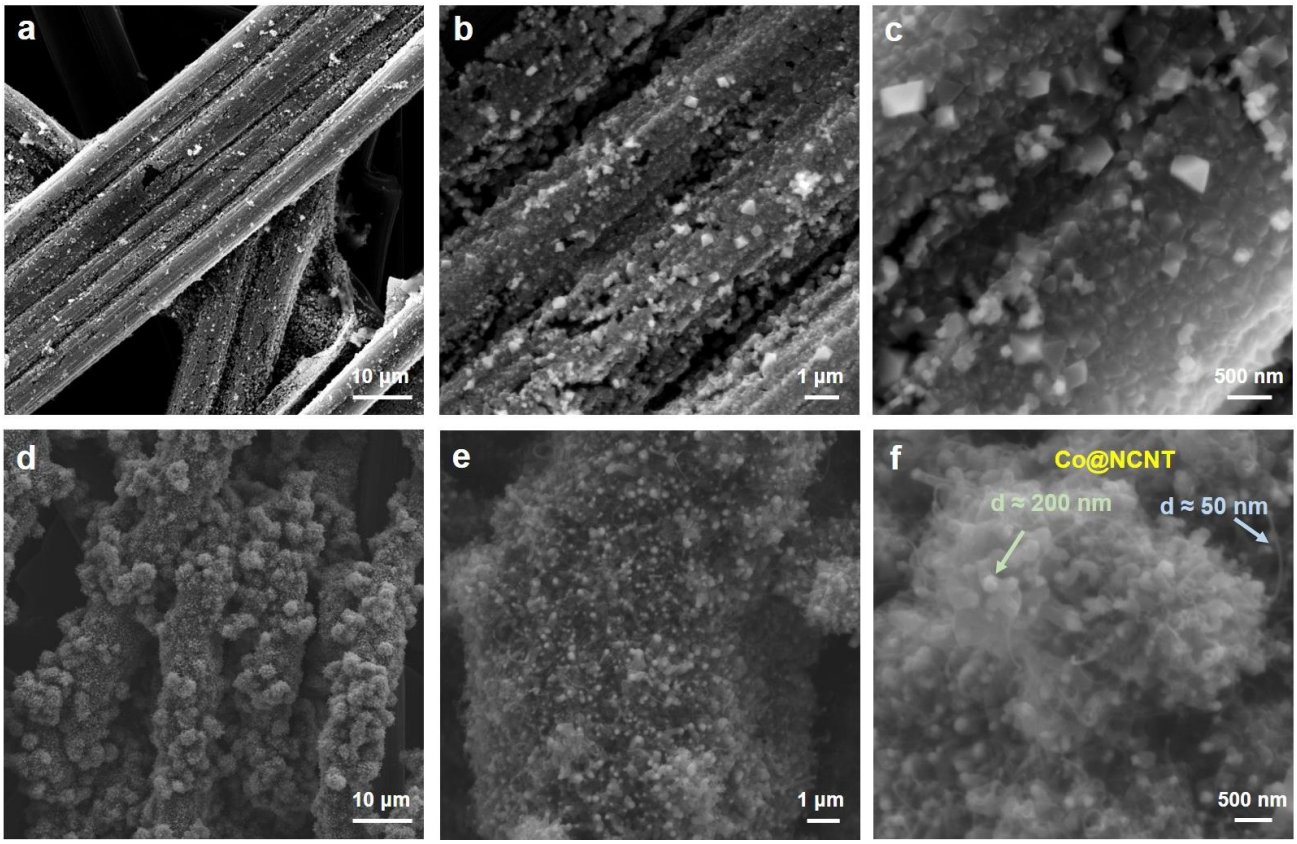

Fig. S14 SEM images of (a-c) CoO and (d-f) Co@NCNT/CoO_x on CFP at different magnifications.

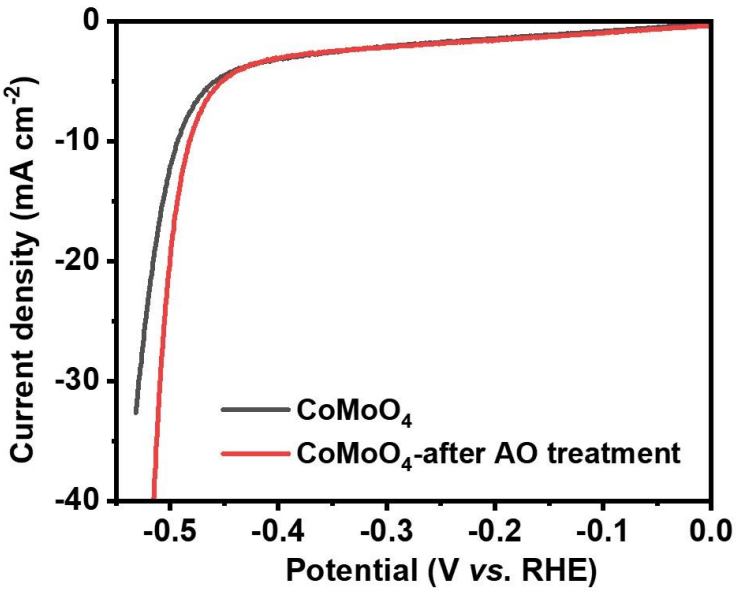

Fig. S15 Polarization curves of pristine $CoMoO_4$ and $CoMoO_4$ after AO treatment.

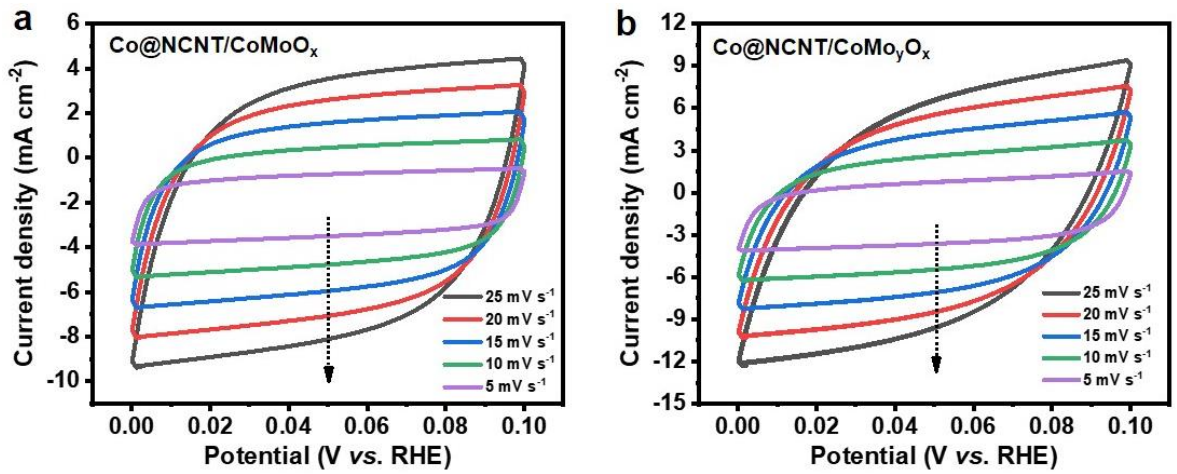

Fig. S16 CV curves of (a) Co@NCNT/$CoMoO_x$ and (b) Co@NCNT/$CoMo_yO_x$ collected at 5, 10, 15, 20, and 25 mV s^{-1} in 1.0 M KOH solution.

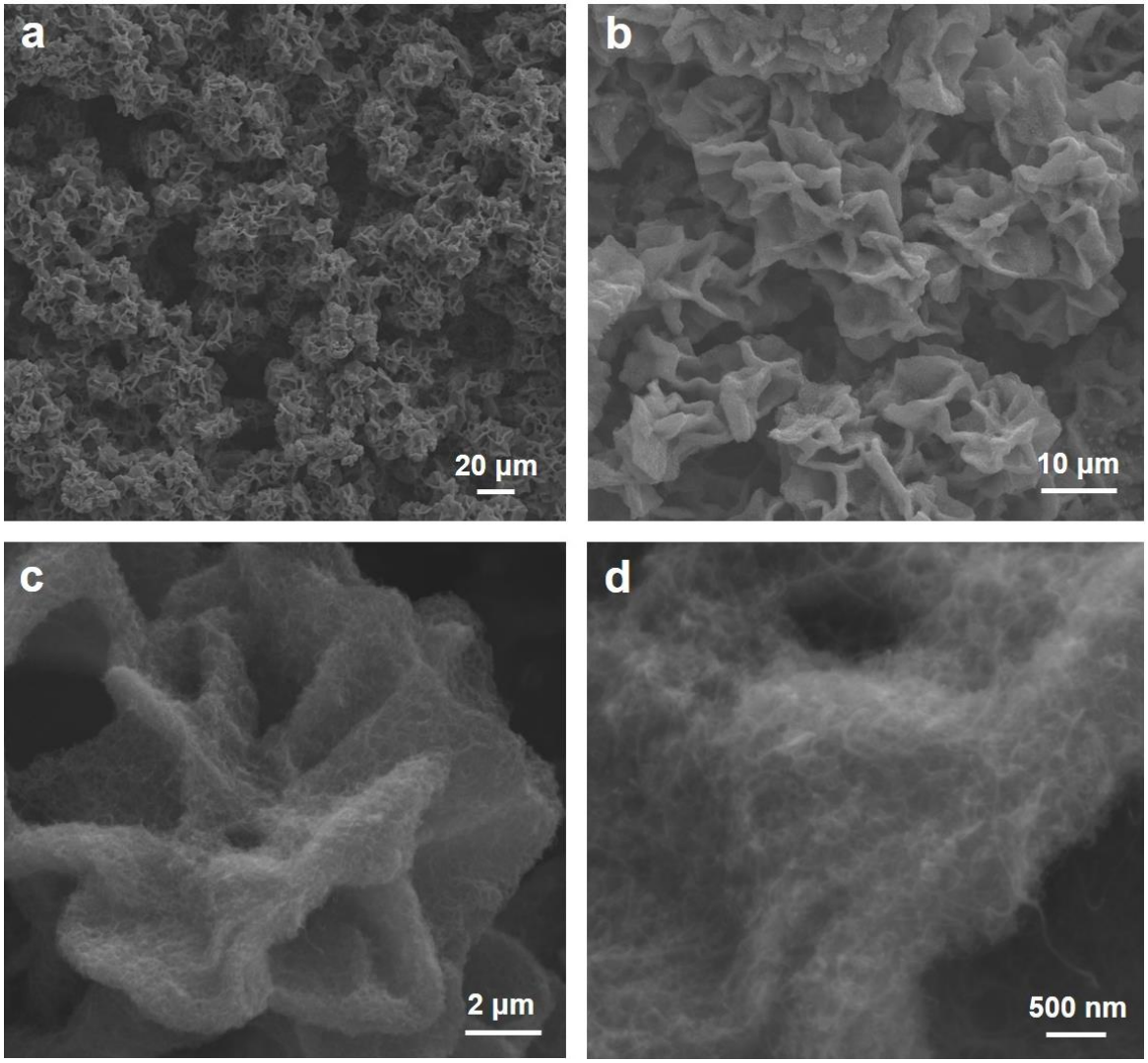

Fig. S17 SEM images of Co@NCNT/$CoMo_yO_x$ at different magnifications.

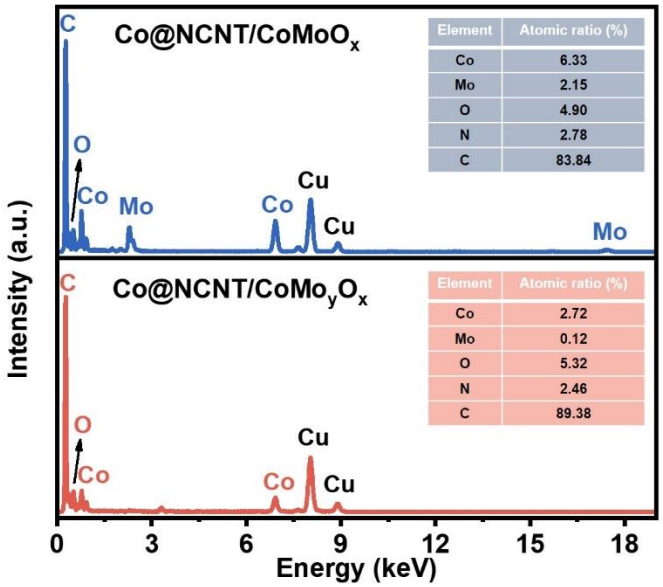

Fig. S18 EDS of Co@NCNT/$CoMoO_x$ and Co@NCNT/$CoMo_yO_x$ (insets: the atomic ratio of Co, Mo, O, N, and C elements).

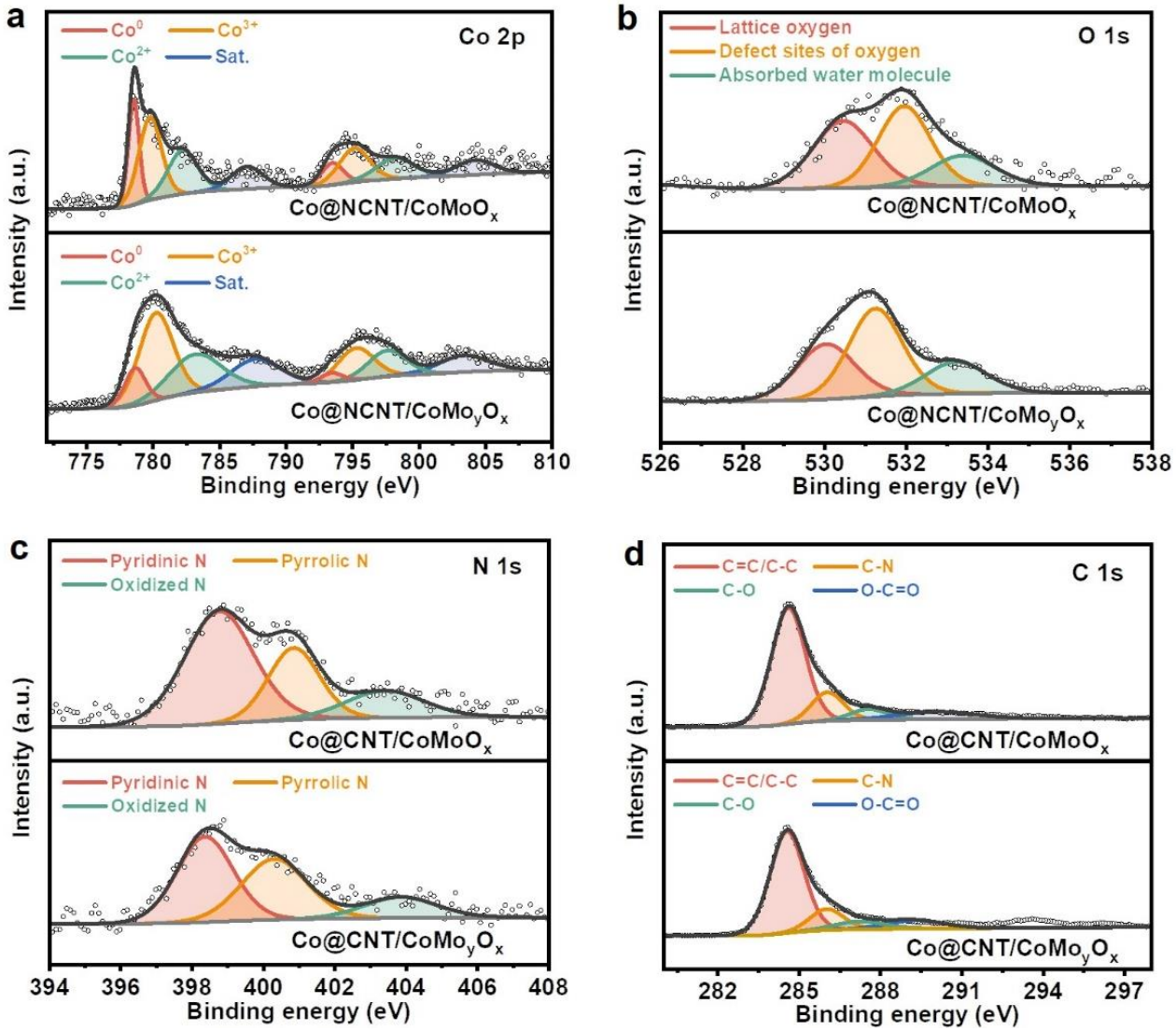

Fig. S19 High-resolution XPS spectra of (a) Co 2p, (b) O 1s, (c) N 1s, and (d) C 1s for Co@NCNT/$CoMo_yO_x$ and Co@NCNT/$CoMoO_x$.

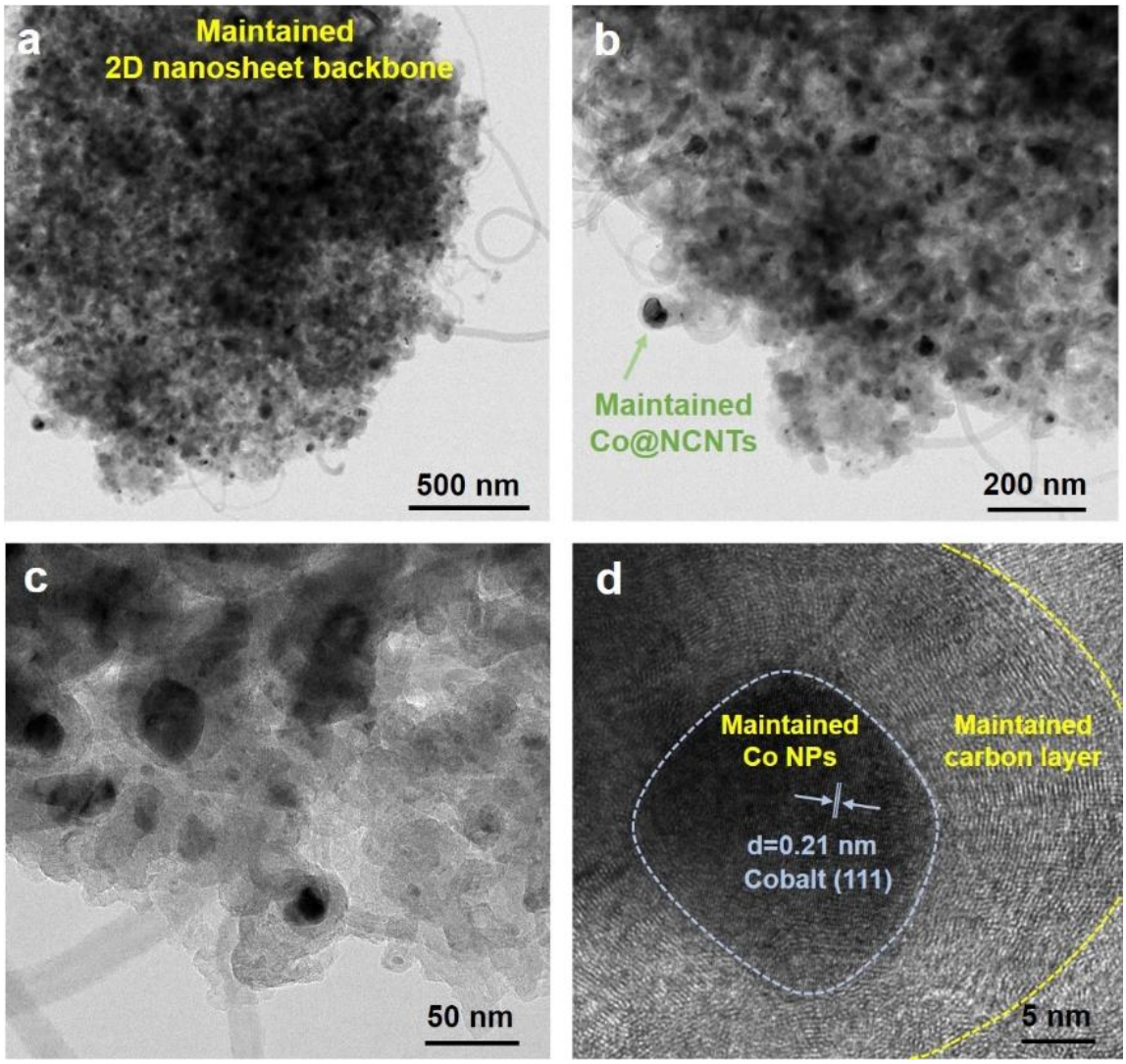

Fig. S20 (a-c) TEM and (d) HRTEM images of Co@NCNT/$CoMo_yO_x$ after the stability test.

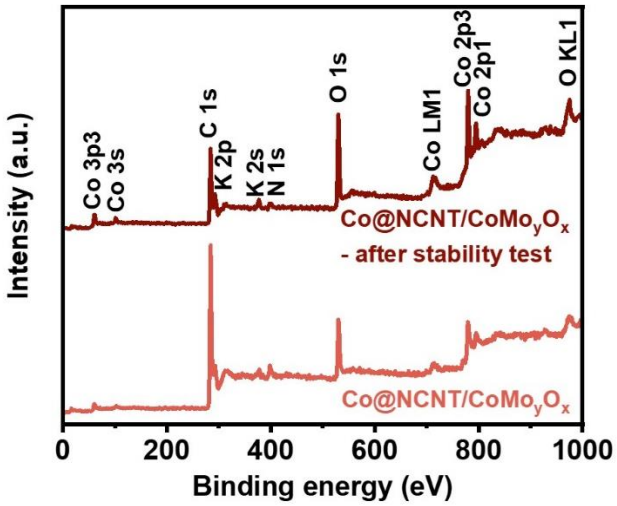

Fig. S21 XPS survey spectra of Co@NCNT/$CoMo_yO_x$ and the Co@NCNT/$CoMo_yO_x$ after the stability test.

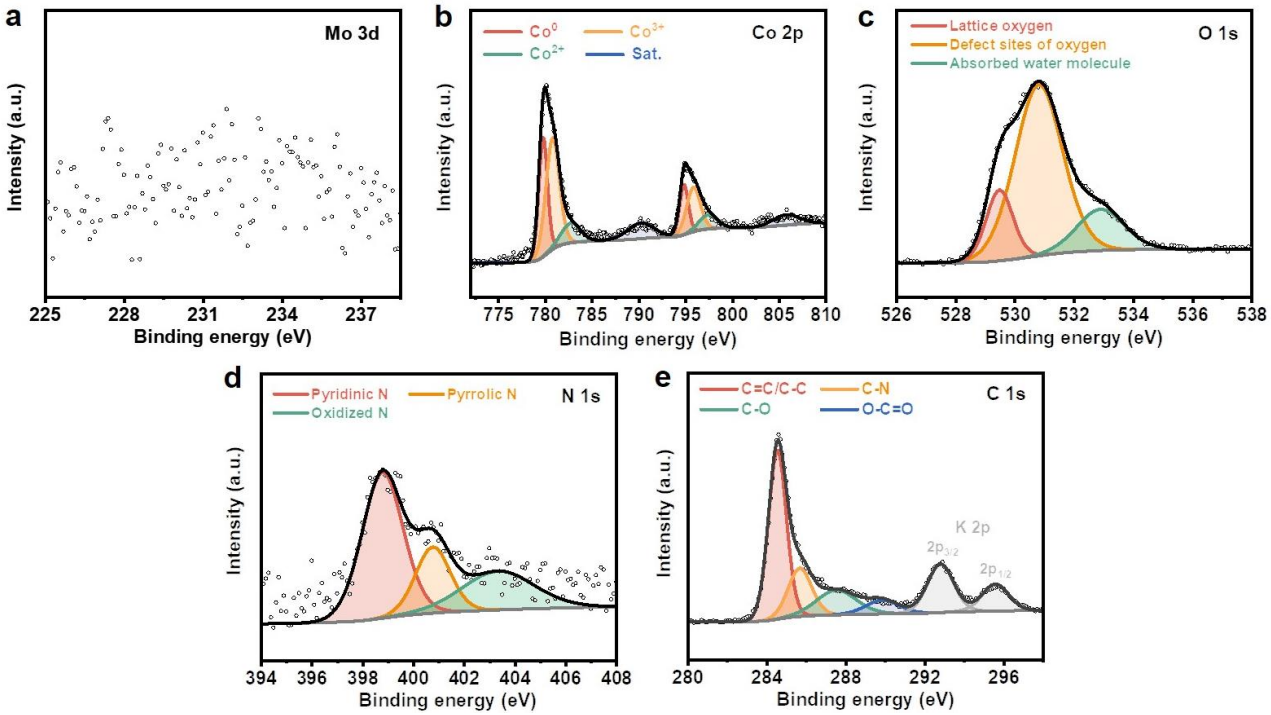

Fig. S22 High-resolution XPS spectra of (a) Mo 3d, (b) Co 2p, (c) O 1s, (d) N 1s, and (e) C 1s for Co@NCNT/$CoMo_yO_x$ after the stability test.

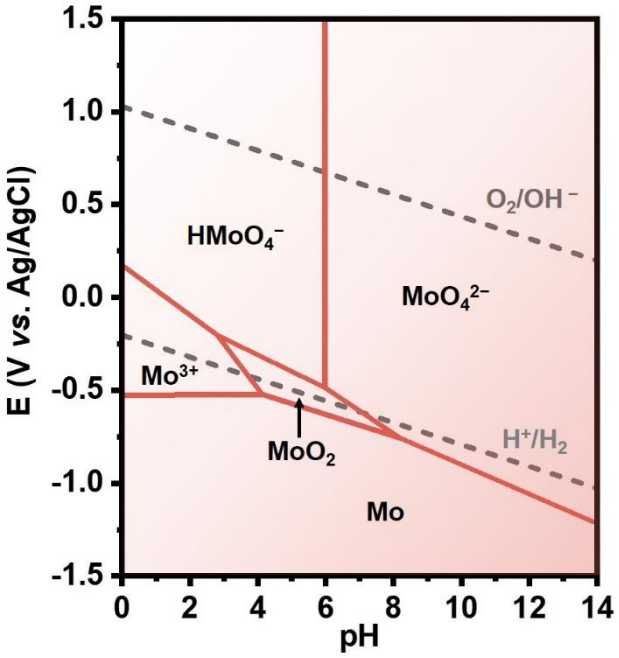

Fig. S23 Pourbaix diagram of Mo in water.[6] The concentration of soluble species is 1.0×10^{-6} mol kg^{-1}.

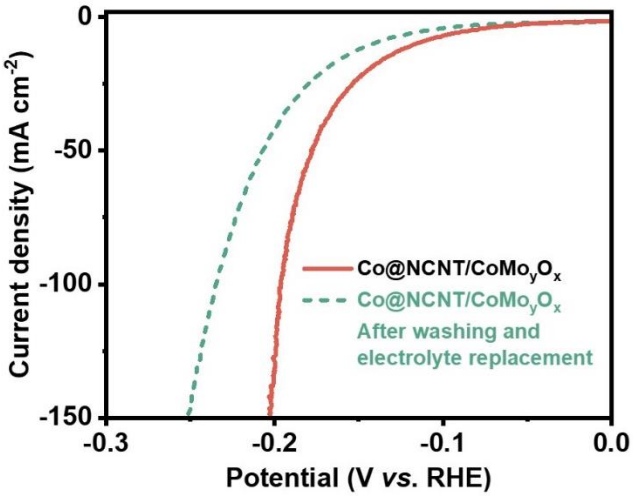

Fig. S24 LSV curve of Co@NCNT/$CoMo_yO_x$ after washing and electrolyte replacement and its comparison with that of as-prepared Co@NCNT/$CoMo_yO_x$.

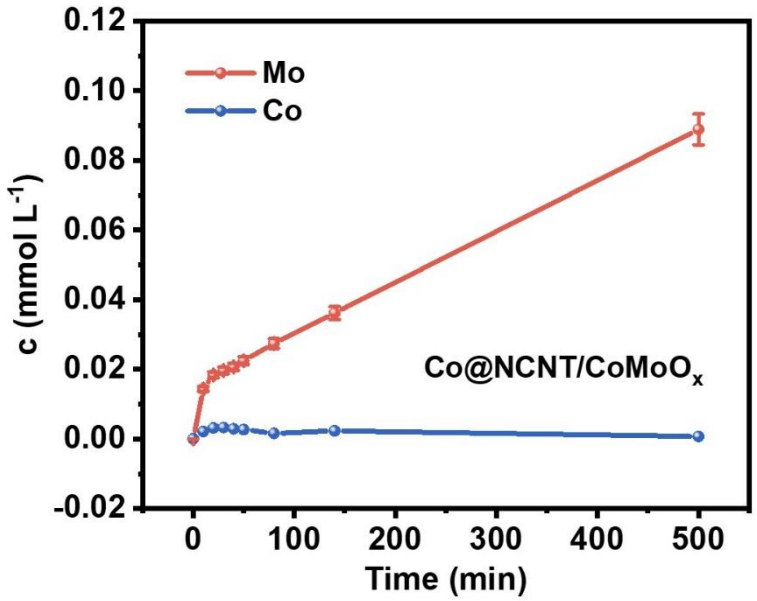

Fig. S25 Time-dependent concentration of dissolved Mo and Co species in the electrolyte of Co@NCNT/$CoMoO_x$ under a CA test at an overpotential of 150 mV.

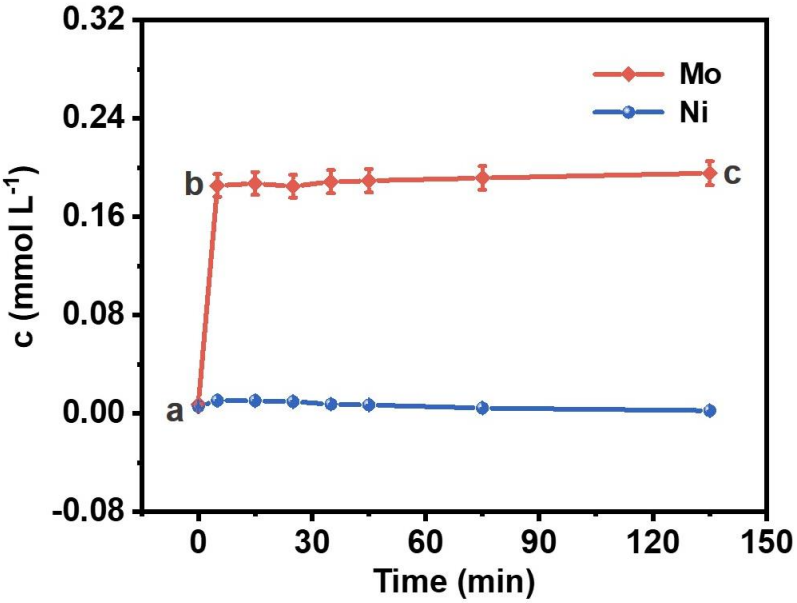

Fig. S26 Time-dependent concentration of dissolved Mo and Co species in the electrolyte of Co@NCNT/$CoMoO_x$ under an AO process (a-b) subsequently combined with a CA test (b-c) at an overpotential of 150 mV.

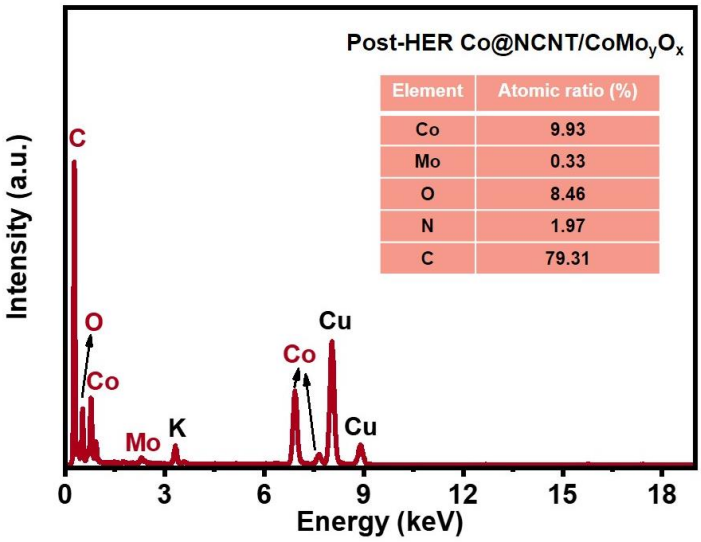

Fig. S27 EDS of post-HER Co@NCNT/$CoMo_yO_x$ to CA test at an overpotential of 150 mV for about 130 min as in above Fig. S23 (insets: the atomic ratio of Co, Mo, O, N, and C elements).

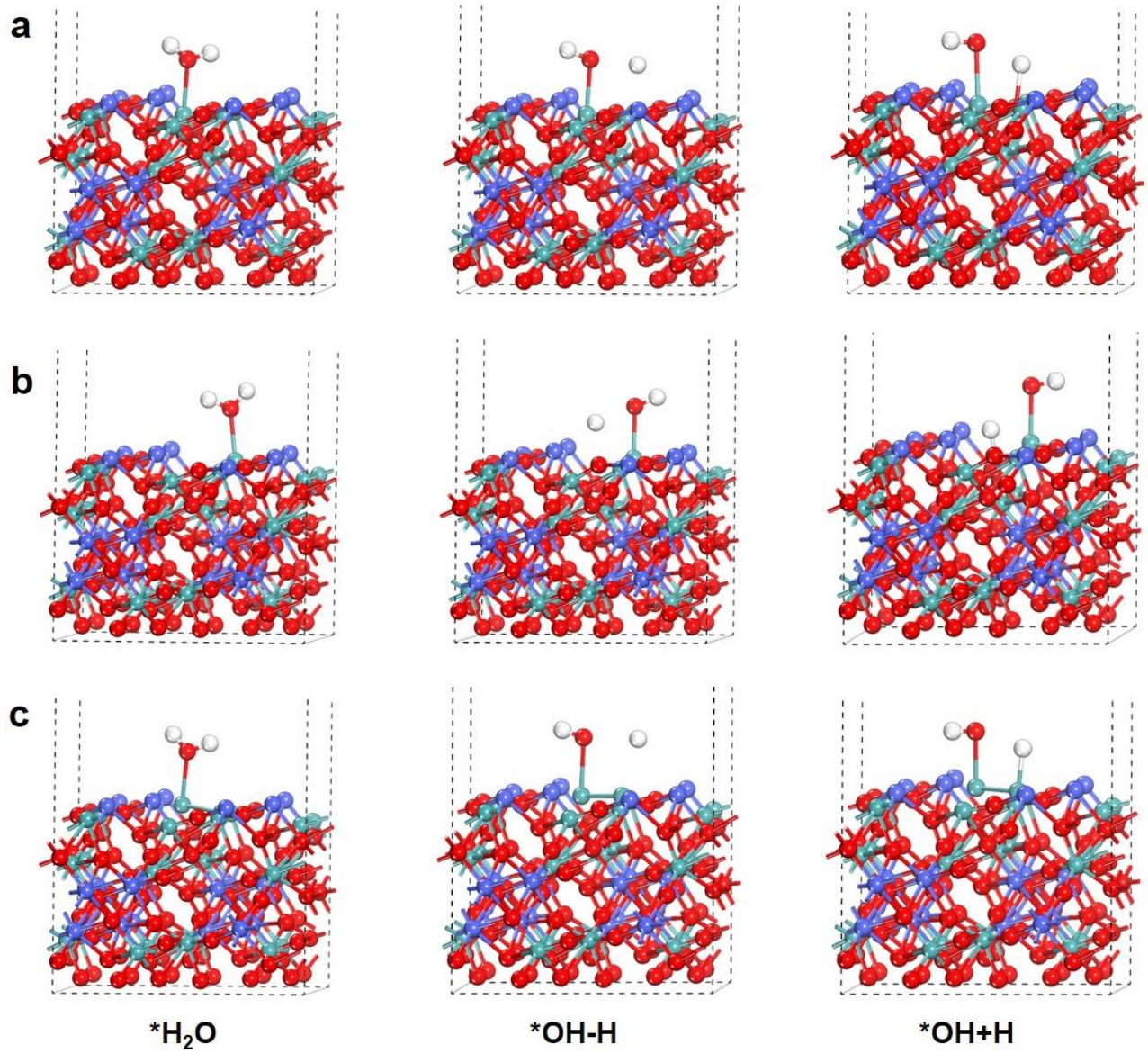

Fig. S28 Atomic configurations of different states of (a) $CoMoO_x$, (b) $CoMo_yO_x$, and (c) $CoMo_yO_x$(Mo-Mo) for the water dissociation. Green, blue, red, and white balls correspond to Mo, Co, O, and H atoms, respectively.

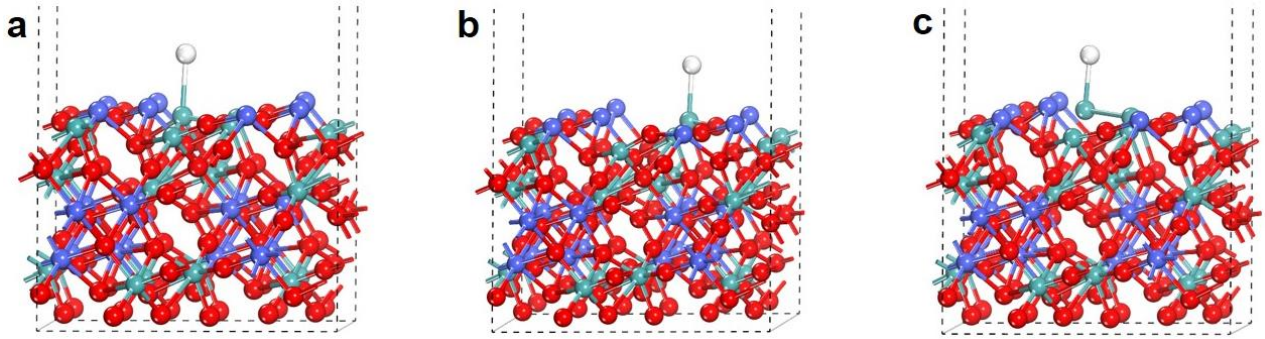

Fig. S29 Atomic configurations of (a) $CoMoO_x$, (b) $CoMo_yO_x$, and (c) $CoMo_yO_x$(Mo-Mo) for the hydrogen adsorption. Green, blue, red, and white balls correspond to Mo, Co, O, and H atoms, respectively.

Table S1. Comparison of the electrocatalytic performance of Co@NCNT/$CoMo_yO_x$ with the previously reported carbon/transition metal-based catalysts for HER in 1 M KOH solution.

Entry	Electrocatalysts	η_{10} (mV)	η_{100} (mV)	Tafel plot (mV dec^{-1})	Durability (h)	References
1	**Co@NCNT/$CoMo_yO_x$**	**94**	**195**	**76**	**600** (CA η=200 mV 400 h η=400 mV 200 h)	***This work***
2	Co/β-Mo_2C@N-CNT	203	/	92	24 (CA η=170 mV)	*Angew. Chem. Int. Ed. 2019, 58, 4923-4928*
3	Co@N-CNTs@rGO	108	~166	64	100 (CA i≈20 mA cm^{-2})	*Adv. Mater. 2018, 30, 1802011*
4	Fe_3C-Co/NC	238	/	109	~16.7 (CA η=238 mV)	*Adv. Funct. Mater. 2019, 29, 1901949*
5	$Ni_{1.5}Co_{0.5}$@N-CNT/ NFs	114	266	117	~12.5 (CA η=200 mV)	*Adv. Sci. 2020, 7, 1902371*
6	C_3N_4@MoN	110	/	58	10 (CA η=110 mV)	*Nano Energy 2018, 53, 690-697*
7	Co-C-N	178	284	102	40 (CA η=170 mV)	*J. Am. Chem. Soc. 2015, 137, 15070-15073*
8	Ni/Mo_2C-NCNFs	143	195	58	100 (CA η=133 mV)	*Adv. Energy Mater. 2019, 9, 1803185*
9	Co-/Ni-MoP@C	162	/	103	10 (CP i=10 mA cm^{-2})	*Nano Energy 2020, 70, 104445*
10	Mo-Co_9S_8@C	113	~336	68	24 (CA η=113 mV)	*Adv. Energy Mater. 2019, 4, 1903137*

Table S2. The fitting results of EIS spectra in alkaline solution.

Sample	R_s (Ω)	CPE-T (S cm^{-2} s^n)	CPE-P (n)	R_{ct} (Ω)
Co@NCNT/$CoMoO_x$	2.12	0.14	0.84	4.26
Co@NCNT/$CoMo_yO_x$	2.16	0.18	0.83	3.10

Table S3. The main composition of the natural seawater used in the work.

Species	Cl^-	Na^+	SO_4^{2-}	Mg^{2+}	Ca^{2+}	K^+
Concentration (mg kg^{-1})	20221	11364	2457	1318	383	402

Table S4. Comparison of the electrocatalytic performance of Co@NCNT/$CoMo_yO_x$ with the previously reported transition-metal-based catalysts for HER in natural seawater.

Entry	Electrocatalysts	η_{10} (mV)	η_{100} (mV)	Durability (h)	References
1	**Co@NCNT/$CoMo_yO_x$**	**125**	**259**	**600** (CP i=10 mA cm^{-2} 400 h i=100 mA cm^{-2} 200 h)	***This work***
2	CoMoC/MXene/NC	262	/	225 (CA η=500 mV)	*Adv. Energy Mater.* **2019**, *9*, 1901333
3	h-MoN@BNCNT	~160	~166	16 (CP i≈10 mA cm^{-2})	*Adv. Funct. Mater.* **2019**, *29*, 1805893
4	Mo_5N_6	257	/	100 (CA η=300 mV)	*ACS Nano* **2018**, *12*, 12761-12769
5	NiCoN|Ni_xP|NiCoN	165	/	24 (CP i=10 mA cm^{-2})	*ACS Energy Lett.* **2020**, *8*, 2681-2689
6	Ni-Mo-S/C	~460	/	/	*Sci. Adv.* **2015**, *7*, e1500259
7	Mn–NiO–Ni/Ni-F	170	/	14 (CA η=140 mV)	*Energy Environ. Sci.* **2018**, *11*, 1898-1910
8	CoMoP@C	~448	/	10 (CA η=500 mV)	*Energy Environ. Sci.* **2017**, *10*, 788-798

References:

1. Kresse, G.; Furthmüller, J. Efficient Iterative Schemes for Ab Initio Total-Energy Calculations Using a Plane-Wave Basis Set. Phys. Rev. B 1996, 54, 11169−11186.
2. Perdew, J. P.; Burke, K.; Ernzerhof, M. Generalized Gradient Approximation Made Simple. Phys. Rev. Lett. 1996, 77, 3865−3868.
3. Kresse, G.; Joubert, D. From Ultrasoft Pseudopotentials to the Projector Augmented-Wave Method. Phys. Rev. B 1999, 59, 1758-1775.
4. Blöchl, P. E. Projector Augmented-Wave Method. Phys. Rev. B 1994, 50, 17953−17979.
5. Grimme, S.; Antony, J.; Ehrlich, S.; Krieg, H. A Consistent and Accurate Ab Initio Parametrization of Density Functional Dispersion Correction (DFT-D) for the 94 elements H-Pu. J. Chem. Phys. 2010, 132, 154104.
6. Nishimoto, M.; Muto, I.; Sugawara, Y.; Hara, N., Morphological Characteristics of Trenching around MnS Inclusions in Type 316 Stainless Steel: The Role of Molybdenum in Pitting Corrosion Resistance. J. Electrochem. Soc. 2019, 166, C3081-C3089.